Simulation of the deformation of polycrystalline nanostructured Ti by computational homogenization

Javier Segurado *, Javier Llorca

A B S T R A C T

Computational homogenization by means of the finite element analysis of a representative volume element of the microstructure is used to simulate the deformation of nanostructured Ti. The behavior of each grain is taken into account using a single crystal elasto-viscoplastic model which includes the microscopic mechanisms of plastic deformation by slip along basal, prismatic and pyramidal systems. Two different representations of the polycrystal were used. Each grain was modeled with one cubic finite element in the first one while many cubic elements were used to represent each grain in the second one, leading to a model which includes the effect of grain shape and size in a limited number of grains due to the computational cost. Both representations were used to simulate the tensile deformation of nanostructured Ti processed by ECAP-C as well as the drawing process of nanostructured Ti billets. It was found that the first representation based in one finite element per grain led to a stiffer response in tension and was not able to predict the texture evolution during drawing because the strain gradient within each grain could not be captured. On the contrary, the second representation of the polycrystal microstructure with many finite elements per grain was able to predict accurately the deformation of nanostructured Ti.

1. Introduction

Titanium and its alloys are well-known engineering materials widely used in many industrial applications including medical devices due to their high corrosion resistance and biocompatibility. In the case of implants, the required mechanical properties cannot always be obtained by alloying and other strategies, such as the modification of microstructure via grain refinement, are options under investigation. For instance, severe plastic deformation (SPD) [1] leads to the formation of ultra fine-grained (UFG) Ti with enhanced mechanical strength. In order to improve further the performance of nanostructured Ti, it is necessary to understand the corresponding deformation mechanisms and to establish models at different length scales that link the microstructure with the mechanical performance. Within this realm, homogenization techniques are very powerful tools to relate the influence of the single crystal properties as well as of the texture on the macroscopic mechanical performance of nanostructured Ti polycrystals taking into account the evolution of the microstructure during deformation.

Notwithstanding that a lot of work has been carried out over the last fifty years on the development of physically-based models of plastic deformation, crystal plasticity modeling and the homogenization of the polycrystal behavior are very active research fields because many issues (i.e. effect of gradients, modeling of twinning or the behavior of grain boundaries) remains still open. The basic ideas of crystal plasticity homogenization were presented in the pioneer work of Taylor [2] and its precise mathematical implementation was developed in the 1960s and 1970s by Hill [3], Rice [4] and Hill and Rice [5]. Since then, the goal was to establish a general theory including a precise formulation for finite deformations [6,7] and an accurate description of the single crystal hardening evolution. Regarding the latter, the first models were phenomenological [8,9] and described the evolution of the critical resolved shear stress (CRSS) of the different slip systems as a function of the accumulated shear strain. More recently, microstructurally-based approaches were aimed at the modeling of hardening from material state variables such as dislocations densities [10–12]. The adoption of a phenomenological or a microstructurally-based hardening model is of secondary importance in so far the actual problem in both cases consists on identifying the correct parameters that reproduce the plastic behavior of a particular single crystal.

In the case of a polycrystal, an interesting option to predict the macroscopic plastic response is the use of homogenization models

based on crystal plasticity models for the grain behavior. The main advantage of these models over standard phenomenological approximations (J_2 theory, etc.) is the ability to include the effect of texture on the anisotropic flow stress and hardening behavior. This is critical in materials which present strong plastic anisotropy or when texture controls the plastic behavior because the initial material is strongly textured or becomes so as a result of large plastic deformations. Several approximations (either analytical or numerical) have been developed to determine the polycrystal behavior and the microstructure evolution during plastic flow. Most analytical formulations are based on the mean field approach and the simplest one is the Taylor model [2] that assumes that all the grains in the polycrystal present the same plastic strain. This leads to a very stiff response and more accurate models were developed in the context of Eshelby's approach [13] and of particular linearization schemes to obtain the polycrystal behavior. Among them, the viscoplastic self-consistent scheme (VPSC) has become the standard tool to homogenize the plastic deformation of polycrystals. This formulation, based on a ad-hoc linearization of the non-linear single crystal constitutive behavior and on the use of the linear self-consistent approximation, was first proposed by Molinari et al. [14] to predict the texture evolution of polycrystalline materials, and it was later extended and implemented numerically by Lebensohn and Tomé [15] in the so-called VPSC code.

Mean-field models (and, particularly, the VPSC approximation) have demonstrated their ability to predict the average flow stress and the texture evolution in polycrystals and they have been recently used to provide constitutive equations for these materials within the context of multiscale simulations [16]. However, these models cannot capture the local stress and strain fields accurately (they generally use only a mean value to represent the distribution of fields inside the grain) and this may lead to large differences *at the local level* for highly anisotropic crystals. In addition, the statistical treatment of the microstructure does not allow to analyze the influence of the actual grain shape and local details of the grain spatial distribution (i.e. clusters of second phases or grain orientations, etc). Under these circumstances, more sophisticated models based on computational homogenization have to be used to capture these local effects. Computational homogenization is based on the numerical simulation of the mechanical behavior of a representative volume element (RVE) of the material microstructure. The numerical solution of the boundary problem is carried out using different techniques, which include the Fast Fourier Transform method [17], recently extended to viscoplastic polycrystals [18], and the finite element method [19,20].

Within this context, the objective of this paper is to tune a computational homogenization model to accurately predict the macroscopic response and texture evolution of nanostructured Ti. Two different approaches will be used to represent the polycrystalline nanostructure Ti. The first is a *voxel* approach in which the RVE is a cube formed by $N \times N \times N$ cubic elements, each one representing one single crystal. The second approximation is based on a *realistic* polycrystalline microstructure in which each crystal is discretized with many cubic finite elements. The accuracy of these two state-of-the-art numerical homogenization strategies to predict the mechanical behavior and texture evolution of polycrystalline nanostructure Ti will be finally compared.

The paper is organized as follows. Section 2 presents the single crystal plasticity model used in the computational homogenization scheme and its numerical implementation in a commercial finite element code. Section 3 is devoted to present the different computational homogenization techniques, while Section 4 includes the simulation results and the corresponding comparison with experimental data.

2. Crystal plasticity model

An implicit implementation of a crystal plasticity model has been carried out in the finite element code ABAQUS [21] as a UMAT subroutine. The mathematical model as well as some details about numerical implementation are described below.

The model assumes a multiplicative decomposition of the deformation gradient into the elastic and plastic components (introduced by Lee and Liu [22] in the context of isotropic plasticity) according to,

$$\mathbf{F} = \mathbf{F}^e\mathbf{F}^p \tag{1}$$

where the configuration defined by $\mathbf{F}^p$ is called the relaxed or intermediate configuration.

From the definition of the velocity gradient, $\mathbf{L}$, expression (1) leads to

$$\mathbf{L} = \dot{\mathbf{F}}\mathbf{F}^{-1} = \dot{\mathbf{F}}^e\mathbf{F}^{e^{-1}} + \mathbf{F}^e\dot{\mathbf{F}}^p\mathbf{F}^{p^{-1}}\mathbf{F}^{e^{-1}} \tag{2}$$

where $\mathbf{L}^p = \dot{\mathbf{F}}^p\mathbf{F}^{p\ -1}$ stands for the plastic deformation rate in the intermediate configuration.

If plastic deformation takes place along multiple slip systems, the plastic velocity gradient $\mathbf{L}^p$ can be obtained as the sum of the shear rates, $\dot{\gamma}^\alpha$, corresponding to each slip system α according to,

$$\mathbf{L}^p = \sum_\alpha \dot{\gamma}^\alpha \mathbf{s}^\alpha \otimes \mathbf{m}^\alpha \tag{3}$$

where $\mathbf{s}^\alpha$ and $\mathbf{m}^\alpha$ stand, respectively, for the unit vectors in the slip direction and perpendicular to the slip plane in the intermediate configuration.

The crystal was assumed to behave as an elasto-viscoplastic solid in which the plastic slip rate for a given slip system follows a power–law dependency,

$$\dot{\gamma}^\alpha = \dot{\gamma}_0\left(\frac{|\tau^\alpha|}{g^\alpha}\right)^{\frac{1}{m}}\mathrm{sign}(\tau^\alpha) \tag{4}$$

where $\dot{\gamma}_0$ is a reference shear strain rate, g^α the critical shear stress on the slip system α, m the rate-sensitivity exponent [23] and τ^α the resolved shear stress on the slip system α.

The elastic strain was defined using the Biot lagrangian strain measure, $\mathbf{E}^e$, given by

$$\mathbf{E}^e = (\mathbf{F}^{\mathbf{e}^T}\mathbf{F}^{\mathbf{e}})^{1/2} - \mathbf{I} \tag{5}$$

where $\mathbf{I}$ stands for the second order identity tensor. The symmetric second Piola–Kirchhoff stress tensor in the intermediate configuration, $\mathbf{S}$, is related with the Biot lagrangian strain according to,

$$\mathbf{S} = \mathbb{C}\mathbf{E}^e \tag{6}$$

where $\mathbb{C}$ stands for the four order elastic stiffness tensor of the single crystal. The resolved shear stress on the slip system α, τ^α, is obtained then by the projection of the Piola stress $\mathbf{S}$, on the corresponding slip system (both defined in the relaxed configuration) as

$$\tau^\alpha = \mathbf{S} : \mathbf{s}^\alpha \otimes \mathbf{m}^\alpha \tag{7}$$

Finally, the Cauchy stress is approximated by

$$\boldsymbol{\sigma} = J^{-1}\mathbf{F}^e\mathbf{S}\mathbf{F}^{\mathbf{e}T} \approx \mathbf{R}^e\mathbf{S}\mathbf{R}^{\mathbf{e}T} \tag{8}$$

under the assumption of small elastic deformations, $\mathbf{R}^e$ being the orthogonal rotation tensor obtained by the polar decomposition of $\mathbf{F}^e$.

The evolution of the critical shear stress g^α for a given slip system, α, was given by

$$\dot{g^\alpha} = h(\Gamma)\dot{\gamma}_\alpha + \sum_{\beta\neq\alpha} q_{\alpha\beta}h(\Gamma)\dot{\gamma}_\beta \tag{9}$$

where Γ is the accumulated shear on all the active slip systems expressed as,

$$\Gamma = \sum_{\alpha} \int |\dot{\gamma}^{\alpha}| \mathrm{dt} \tag{10}$$

where $q_{\alpha\beta}$ stands for the latent hardening coefficients and $h(\Gamma)$ is the hardening modulus. The phenomenological Voce hardening model – adapted for single crystals – is used for $h(\Gamma)$, according to [24]

$$h(\Gamma) = h_0 + \left(h_0 - h_s + \frac{h_0 h_s \Gamma}{\tau_s}\right) \exp^{-h_0 \Gamma / \tau_s} \tag{11}$$

Hardening in this model depends on four parameters, namely the initial critical resolved shear stress $g^{\alpha}(\Gamma = 0) = \tau_0$, the saturation shear stress τ_s and the initial (h_0) and saturation (h_s) hardening moduli. The model is able to reproduce the typical plastic behavior of single crystals including stage I and II hardening.

2.1. Numerical implementation

The model described above has been implemented in the finite element code Abaqus/Standard as a user material subroutine using a backward Euler implicit scheme. The starting point to obtain the response in any integration point at time $t + \Delta t$ is the solution at time t which is given by elastic deformation gradient, $\mathbf{F}_t^e$, and the plastic shear strains, γ_t^{α}. In addition, a prediction of the deformation gradient in $t + \Delta t$, $\mathbf{F}_{t+\Delta t}$, is given by the finite element solver based on the global tangent stiffness. From these values, the subroutine solves a set of non-linear algebraical equations formed by the discretization in time of Eqs. 4, 7, 9 and 11. This is carried out by the minimization of a residual function $\mathbf{R}$ [25],

$$\mathbf{R}(\mathbf{F}^e_{t+\Delta t}) = \mathbf{F}^e_{t+\Delta t} - \mathbf{F}_{t+\Delta t}\mathbf{F}_t^{-1}\mathbf{F}_t^e \exp\left[-\Delta t \sum_{\alpha} \dot{\gamma}^{\alpha}(\mathbf{F}^e_{t+\Delta t})\mathbf{s}^{\alpha} \otimes \mathbf{m}^{\alpha}\right] \tag{12}$$

where the exponential map operator, exp, has been used to integrate the evolution of plastic deformation gradient over the time increment. The minimization procedure is performed using a Newton–Raphson scheme which incorporates an analytical evaluation of the Jacobian matrix (derivatives of $\mathbf{R}$). The function g^{α} for each slip system is updated using the corresponding hardening laws (11) during the iterative procedure, leading to the updated values of $\mathbf{F}^e$,$\boldsymbol{\sigma}$ and of the internal variables γ^{α} in $t + \Delta t$. In addition, the elasto-plastic tangent stiffness matrix –required by the finite element solver to carry out the global iteration procedure– was obtained following the numerical procedure detailed in [26].

2.2. Particularization to nanostructured Ti

Ti is an HCP material and its elastic behavior is defined by 5 independent constants [27]: C_{11} = 162.4 GPa, C_{33} = 180.7 GPa, C_{44} = 117 GPa, C_{66} = 35.2 GPa, C_{12} = 92 GPa and C_{13} = 69 GPa.

Plastic deformation of Ti occurs by slip along prismatic, basal and two pyramidal systems as well as by tension and compression twinning [28]. Nevertheless, the stress necessary to activate twinning increases rapidly as the grain size decreases [29] and twinning does not occur when the grain size is below 1 μm. As a result, plastic deformation of nanostructured Ti is dominated by plastic slip and the crystal plasticity model included three $\{0001\}\langle 11\bar{2}0\rangle$ basal slip systems, three $\{10\bar{1}0\}\langle 11\bar{2}0\rangle$ prismatic systems, six $\{10\bar{1}1\}\langle 11\bar{2}0\rangle$ a pyramidal systems, and 12 $\{10\bar{1}1\}\langle 11\bar{2}3\rangle c+a$ pyramidal systems. However, the activity of the a pyramidal system at room temperature is very small and this system was not included in the simulations [30].

The critical resolved shear stress (CRSS) of each slip system in Ti is highly dependent on the material purity [28]. In addition, most of the experimental data on the CRSS were measured by testing suitably-oriented large single crystals but these results cannot easily be extrapolated to obtain the properties of the grains in the polycrystal due to the differences in the processing route and in grain size. An alternative procedure was recently developed by Gong and Wilkinson [30], who measured the single crystal properties of commercially pure (CP) Ti by means of mechanical tests of micron-sized cantilever beams sculpted by focused ion beam inside of crystallites of a polycrystalline sample. The microbeams – oriented to undergo single slip in a given system – were loaded in bending with a nanoindenter and the CRSS of the different slip systems were obtained for beams of 4 μm in depth. Although it is well known that these values may not be representative of the actual ones in CP nanostructured Ti because of the smaller grain size, it can be assumed the grain size influences in a similar way to all slip systems. Under this assumption, the ratios of the CRSS between different slip systems can be considered size independent and can be obtained from [30], leading to $\tau^{basal} = 1.155\tau^{prismatic}$ and $\tau^{pyramidal} = 2.618\tau^{prismatic}$. The rest of the material parameters which control the plastic deformation of CP nano structured Ti were chosen to fit the experimental results presented in Section 4.

3. Computational polycrystal homogenization framework

The effective properties of CP polycrystalline nanostructured Ti were determined by means of the finite element simulation of an RVE of the microstructure. Two different representation of the microstructure were used. The first one is a voxel-based model in which the RVE is made up by a regular mesh of *NxNxN* cubic finite elements, Fig. 1a. Each cubic element stands for a Ti single crystalline grain and thus the model can include a large number of grains. While this is important from the statistical viewpoint, this representation of the microstructure leads to a poor description of the grain shape and of the strain fields within the grains as a linear displacement interpolation is used in each cubic finite element.

Another possibility to represent the microstructure is depicted in Fig. 1b. The finite element discretization was also carried out with cubic elements but each crystal was represented with many elements and, thus, the model includes information about the distribution of grain sizes and shapes within the polycrystal. In addition, complex deformation fields can be accounted for within each grain. The actual microstructure can be obtained from experimental data provided by sequential serial sectioning or X-ray microtomography [31] or from synthetic microstructure generators. In this case, the open-source code Dream3D [32] was used to create the RVE shown in Fig. 1b. The grains were equiaxed and their size followed a lognormal distribution with an average grain volume equal to the RVE volume divided by 100. Obviously, this representation is more accurate than the previous one but the computational cost limits the number of crystals in the model. In either RVE of the polycrystal, the orientation of the each grain was determined from the orientation distribution function (ODF) which describes the initial texture using a Monte Carlo lottery. Thus, the texture of the RVE can be considered representative of the actual polycrystal texture if the number of grains in the RVE is large enough.

The effective polycrystal behavior is obtained by computational homogenization from the numerical simulation of an RVE of finite size. It is nowadays well established that the best results are obtained if periodic boundary conditions are applied to the RVE [33] because the effective behavior derived under these conditions is always closer to the exact solution (obtained for an RVE of infinite size) than those obtained under imposed displacements or forces.

Periodic boundary conditions assume that the whole RVE deforms as a jigsaw puzzle and that a periodic translation of the

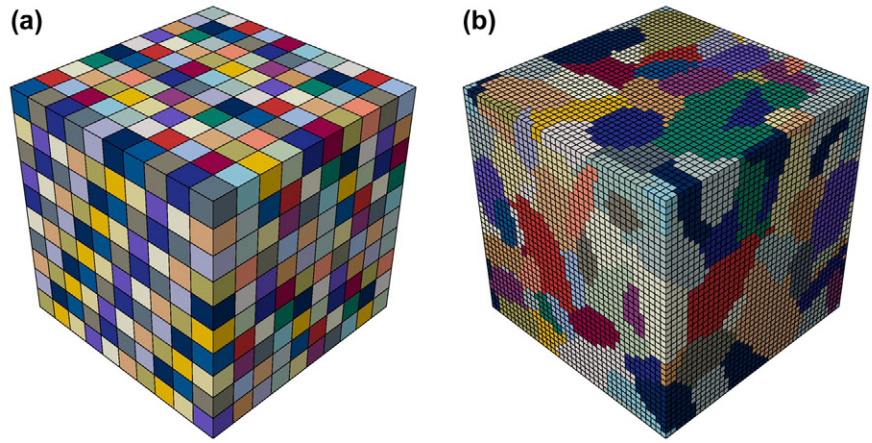

Fig. 1. Representative volume elements of polycrystalline Ti. (a) Voxel model with 1000 cubic finite elements in which each one stands for a single crystal. (b) Realistic RVE containing 100 crystals discretized with 64000 cubic finite elements.

RVE in the three directions fill the whole space. If the three concurrent edges of the cubic RVE define an orthogonal basis $\mathbf{e}_1$, $\mathbf{e}_2$ and $\mathbf{e}_3$ with corresponding coordinates x_1, x_2, x_3, the periodic boundary conditions link the local displacement vector $\mathbf{u}$ of the nodes on opposite faces of the cubic RVE with the far-field macroscopic deformation gradient $\overline{\mathbf{F}}$ according to,

$$\begin{aligned}\mathbf{u}(x_1,x_2,0)-\mathbf{u}(x_1,x_2,L)&=(\overline{\mathbf{F}}-\mathbf{I})\mathbf{L}_3\\ \mathbf{u}(x_1,0,x_3)-\mathbf{u}(x_1,L,x_3)&=(\overline{\mathbf{F}}-\mathbf{I})\mathbf{L}_2\\ \mathbf{u}(0,x_2,x_3)-\mathbf{u}(L,x_2,x_3)&=(\overline{\mathbf{F}}-\mathbf{I})\mathbf{L}_1\end{aligned} \tag{13}$$

where L is the cube length, and $\mathbf{L}_i = L\mathbf{e}_i$. These boundary conditions are implemented in the finite element simulation by means of multipoint constraints which link the displacement of each pair of opposite cube faces. The far-field deformation gradient $\overline{\mathbf{F}}$ applied to the boundaries of the RVE is given by

$$\mathbf{u}(M_i)=(\overline{\mathbf{F}}-\mathbf{I})\mathbf{L}_i \tag{14}$$

where $\mathbf{u}(M_i)$ stand for the prescribed displacements in three master nodes M_i corresponding to three different faces of the RVE. If some components of the far-field deformation gradient are not known *a priori* (e.g. under uniaxial tension), the corresponding effective stresses $\bar{\boldsymbol{\sigma}}$ are set instead. This is carried out by applying nodal forces P_j to the corresponding master node M_i and degree of freedom j according to

$$P_j(M_i)=(\bar{\boldsymbol{\sigma}}\mathbf{e}_i)_j A_i \tag{15}$$

where A_i is the current area of the face perpendicular to $\mathbf{e}_i$.

4. Numerical results

The simulation strategy presented was used to simulate the behavior of CP nanostructured Ti produced by ECAP-C (equal channel angular pressing-conform). ECAP-C is a severe plastic deformation process in which a metal billet is pulled through a channel following the scheme depicted in Fig. 2. The process leads to the manufacturing of long billets of metallic materials with UFG microstructure. The billet is normally subjected to several passes and is rotated 90° after each pass to obtain a more isotropic texture. The reference system used for the ECAP-C processing x_1, x_2 and x_3 is also indicated in Fig. 2 and will be used later to define the texture orientation and the loading paths for both tensile deformation and drawing.

Processing and mechanical testing of the material was performed in the Institute of Physics of Advanced Materials, Ufa State Aviation Technical University, Russia and is detailed in [34]. The starting material was a CP Ti (Grade 4) in form of billets and it was subjected to ECAP-C processing at 200 °C for different number of passes (in the range 1–10). The average grain size after four passes or more was approximately 300 nm.

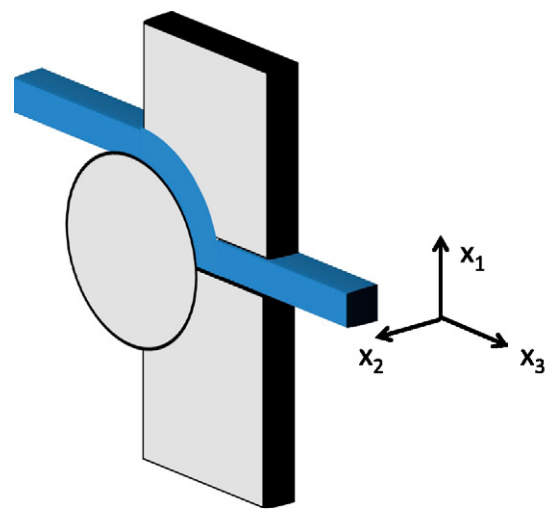

Fig. 2. Schematic of the ECAP-C process.

4.1. Tensile deformation of nanostructured Ti

The tensile behavior in the x_3 direction was measured experimentally after different number of ECAP-C passes, and the material response after four ECAP-C passes was simulated with the two polycrystalline models described above. In the first approach, Fig. 1a, an RVE with 1000 crystals was selected because the number of orientations was enough to give a very small scatter on the predicted stress–strain response. In the second approximation, Fig. 1b, 100 grains were represented by means of 64,000 cubic elements. It was checked that increasing the number of elements to represent each grain did not substantially change the accuracy of the solution. The final size of this model (100 crystals and 640 elements per crystal) was a compromise between accuracy and computational cost: 24 h in a 4-core computer were necessary to simulate the tensile response up to an applied engineering strain of 1.

The starting point of the simulation was the generation of a distribution of crystal orientations to be used in the polycrystalline

models. Orientation distribution functions (ODF) were obtained by X-ray diffraction after the four ECAP passes [34] and the resulting pole figures in the rod direction (x_3) are shown in Fig. 3a. From that experimental ODF equivalent textures were generated using a Monte Carlo lottery where the probability of a random orientation is weighted to reproduce the original ODF. The resulting pole figures are depicted in Fig. 3b for 1000 crystals (corresponding to the first model) and in Fig. 3c for 100 crystals (corresponding to the second approach). Both synthetic pole figures reproduce the main features of the experimental ODF although the limited number of crystals in the model (particularly for 100 grains) influences the roughness of the pole figures and the maximum intensities.

The plastic behavior of the single crystals was based on the CRSS ratios measured by [30]. In addition, the CRSS of each slip system was taken as the saturation stress in the Voce hardening model (τ_s^α) and $\tau_0^\alpha = 0.9\tau_s^\alpha$. Secondly, the hardening rates were identical for the three active slip systems ($h_0^\alpha = h_0$ and $h_s^\alpha = h_s$ for all α).The hardening was assumed to be isotropic and thus $q_{\alpha,\beta} = 1$. And, finally, the reference shear strain rate $\dot{\gamma}_0$ was taken to be equal to the applied strain rate in the experiments with a rate-sensitivity exponent $m = 0.1$. Under these assumptions, only three independent parameters were necessary to fit the experimental data: h_0, h_s and a proportionality factor for all the normalized CRSSs. Fitting of these parameters was carried out using a trial and error strategy with the model with 1000 cubic crystals because of the lower computational cost. The resulting parameters for CP nanostructured Ti single crystals are shown in Table 1.

Table 1
Parameters defining the mechanical behavior of the slip systems in single crystals of CP nanostructured Ti.

Slip system	τ_0 (MPa)	τ_s (MPa)	h_0 (GPa)	h_s (GPa)
Prismatic	232.9	258.7	2.5	89.1
Basal	268.9	298.8	2.5	89.1
Pyramidal $a+c$	609.8	677.6	2.5	89.1

Two models for each type of polycrystalline representation of the RVE were generated. In the case of the voxel model with 1000 crystals, the two realizations differed in the initial crystal orientations within the RVE. In the case of RVE with 100 grains, the two models differed in the particular grain distribution and in the initial crystal orientations but the grain shape (equiaxial) and size were kept.

Periodic boundary conditions were applied in all cases. The four models were subjected to tensile deformation in the rod direction (corresponding to the x_3 axis of the textures represented in Fig. 3). The applied strain rate $\dot{\epsilon}$ was equal to the reference shear strain rate $\dot{\gamma}_0$. The final deformation applied was 100%, corresponding to a logarithmic strain $\epsilon = 0.69$. Thus, the applied deformation history for the simulation of the tensile tests, following Eq. (13), is given by

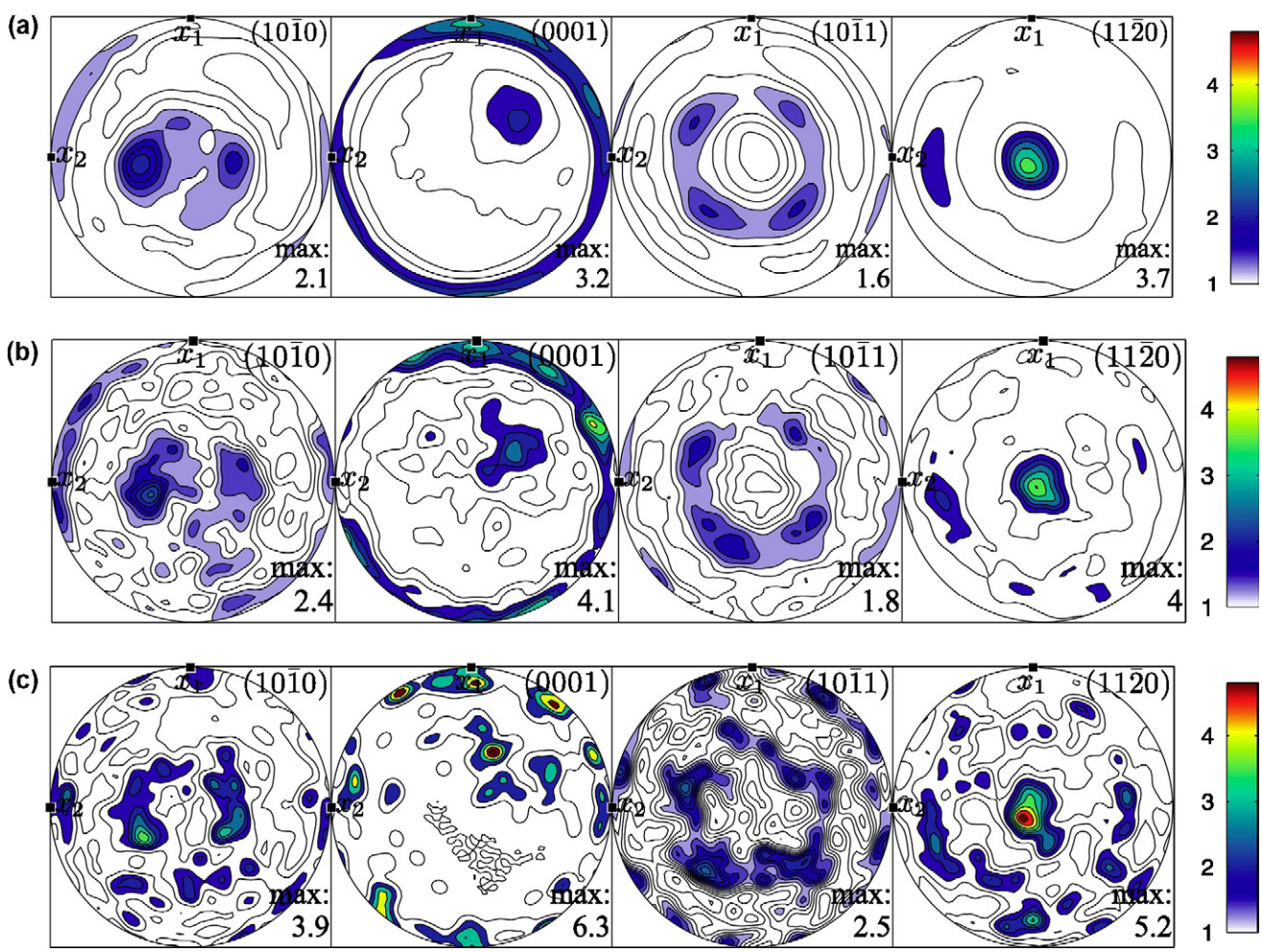

Fig. 3. Pole figures of CP nanostructured Ti in the rod direction (x_3) after four ECAP-C passes. (a) Pole figures of experimental ODF. (b) Pole figures obtained from experimental ODF using Monte Carlo lottery for 1000 crystals. (c) *Idem* for 100 crystals.

$$
\begin{aligned}
&\dot{u}_3(M_3) = \dot{\epsilon} L_0 \\
&P_1(M_3) = P_2(M_3) = 0 \\
&P_i(M_1) = P_i(M_2) = 0, \quad i = 1,2,3
\end{aligned}
\tag{16}
$$

The effective Cauchy stress of the polycrystal was obtained as the applied load on face x_3 divided by current face area and the results of the four models are plotted as a function of the applied strain in Fig. 4, together with the experimental data. The models based in one voxel for each crystal were able to reproduce very accurately the experimental curve, although this agreement is obviously a consequence of the fitting of the single crystal properties to the experimental data. It is worth noting that the curves of the two voxel models were superposed, indicating that the size of the RVE (made up of 1000 crystals) was large enough to provide a response representative of the macroscopic behavior. The finite element models corresponding to 100 grains with realistic shape showed a softer response and the flow stress was around 5% lower than that computed with the models with one voxel per grain. As the single crystal properties were identical in all cases, these disparities should be attributed to the differences in the representation the microstructure. The models in which each grain is represented by one single element provide a stiffer response because the deformation is overconstrained to maintain the compatibility between adjacent crystals. This fact is enhanced by the poor representation of the strain fields because the linear finite elements cannot reproduce the strain concentrations on the grain surfaces. In addition, the localization of plasticity in slip bands is hindered, leading to a more homogeneous plastic strain distribution. This is shown in Fig. 5a and b, which depict the contour plots of the accumulated plastic slip Γ for both model types after a logarithmic strain $\epsilon = 0.69$. For the reasons indicated above, the model based in one voxel per grain was not able to capture the localization of plastic deformation within the grains, leading to a stiffer response. The effect of the discretization of each grain with many finite elements has been previously studied for FCC materials [35] and the results obtained here for a nano-grained HCP metals are in concordance with those studies.

It should be finally noted the slight difference (around 3%) in the flow stress between the two finite element models with a realistic microstructure. This behavior is very likely due the limited number of grains in the RVE (100 crystals), which leads to noticeable statistical differences between them.

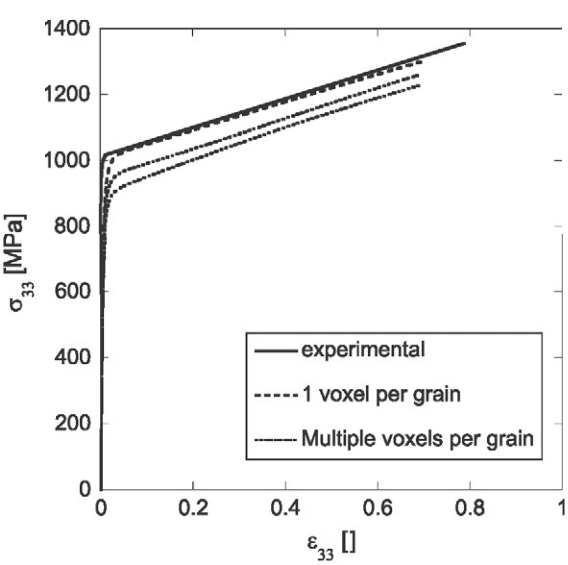

Fig. 4. Tensile stress–strain curves in the x_3 direction: experimental results from [34] and numerical simulations using the two representations the polycrystal, one-voxel per grain model and multivoxel per grain model.

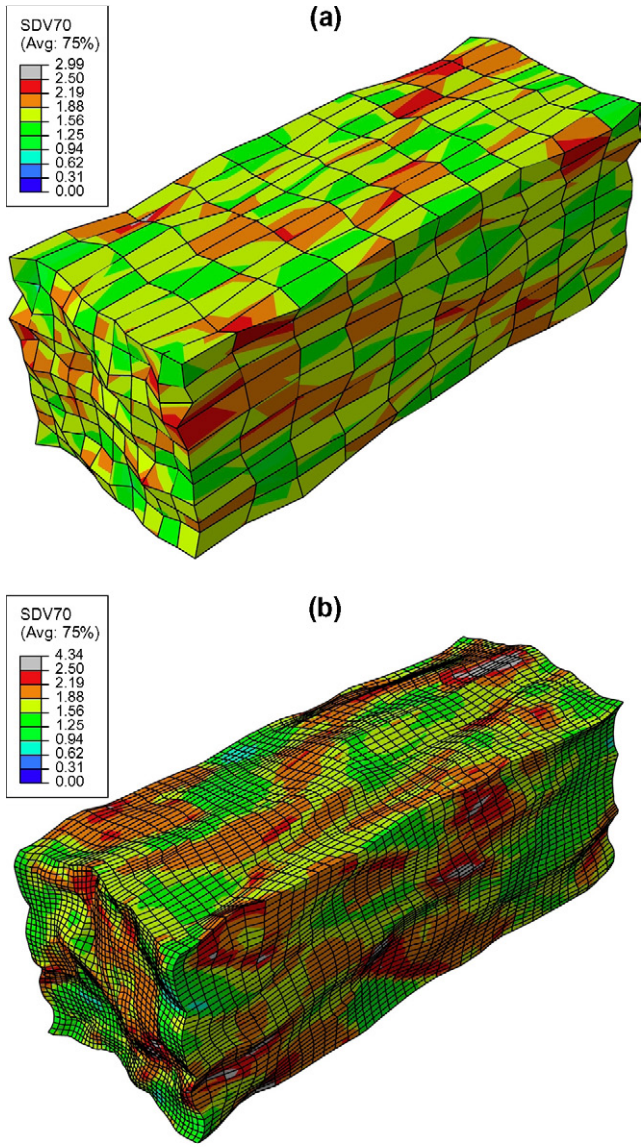

Fig. 5. Contour plot of the accumulated plastic slip Γ in the microstructure of polycrystalline Ti after 100% of tensile strain. (a) RVE containing 1000 crystals, each one represented by one cubic finite element. (b) RVE containing 100 crystals, each one represented with 640 cubic finite elements.

4.2. Simulation of the drawing process after ECAP

The drawing process was simulated in order to check the ability of the two models to predict the evolution of texture and the simulation results were compared with the experimental textures after drawing. The nanostructured Ti billets produced in [34] after six ECAP-C passes were subjected to drawing at 200 °C to produce rods with the longitudinal axis oriented in x_3 direction (Fig. 2). The material was not tested at 200 °C so no actual data were available for the single crystal properties at this temperature. However, the ratios between critical resolved shear stresses were found to remain constant from room temperature up to 500 K [28]. Under these circumstances, the texture evolution can be accurately predicted using the parameters obtained at ambient temperature for the single crystal behavior although the actual stress values could be overestimated.

The drawing process was idealized by the application of a strain history to the RVE that corresponds to the one underwent by the material at the center of the rod. Let x_3 be the drawing direction while x_1 and x_2 are perpendicular axes contained in the cross section of the rod, as depicted in Fig. 2. The applied strain history consists of equi-biaxial compression along the directions x_1 and x_2 while the rod is stress free along the $x-3$ axis. This stress state was obtained by imposing the same velocities $\dot{u}$ on the master nodes controlling the deformation of faces 1 and 2, according to (Eq. (13)),

$$\begin{aligned} &\dot{u}_1(M_1) = \dot{u}_2(M_2) = \dot{u} = -\dot{\epsilon}L_0 \\ &P_2(M_1) = P_3(M_1) = P_1(M_2) = P_3(M_2) = 0 \\ &P_i(M_3) = 0, \quad i = 1,2,3 \end{aligned} \tag{17}$$

The applied strain rate $\dot{\epsilon}$ was chosen to be equal to the reference shear strain rate $\dot{\gamma}_0$. The experimental drawing process led to reduction from billets with a cross section of $11 \times 11\ \text{mm}^2$ to a rod with 6 mm in diameter. This reduction of area corresponds, in average, to a reduction of the RVE length in directions x_1 and x_2 of $L_1 = L_2 = 0.483L$, being L the initial length of the cubic RVE sides. Finally, the texture used as starting point for the simulation of the drawing process was the one resulting after six ECAP-C passes, essentially identical to the one after four passes depicted in Fig. 3.

The texture measured by X-ray diffraction after the drawing process and the corresponding results of simulations are shown in Fig. 6.

The experimental texture (Fig. 6a) corresponds to a $(10\bar{1}0)$ fibre texture along the rod axis (direction x_3). Such texture is typical of CP Ti after swaging and/or drawing. The texture predictions obtained with the model in which each crystal is represented by one cubic finite element, Fig. 6b, failed to predict the experimental texture: the pole figures predicted for directions $(10\bar{1}0)$ did not present a maximum in the x_3 direction but in a ring surrounding that direction (at an angle of approximately 10°). On the contrary, the pole figures of the polycrystal model in which each grain was represented by 640 cubic elements, Fig. 6c, predicted very accurately the experimental texture (both qualitatively and quantitatively).

The differences in the texture predictions between both types of representations of the microstructure can be traced again to the ability of each model to represent the deformation fields inside the grains. The actual orientation of each integration point in the FE model is obtained from the elastic rotation tensor $\mathbf{R}^e$ (provided by the polar decomposition of the elastic deformation gradient $\mathbf{F}_e$) that is linearly interpolated across the element. Thus, the crystal orientation is characterized by 8 values (corresponding to the 8 Gauss points) if the single crystal is represented with one element, and the orientation can only vary linearly within the element.

In order to show the real distribution of orientations in grains, Fig. 7 shows the third Euler angle at each element when each grain

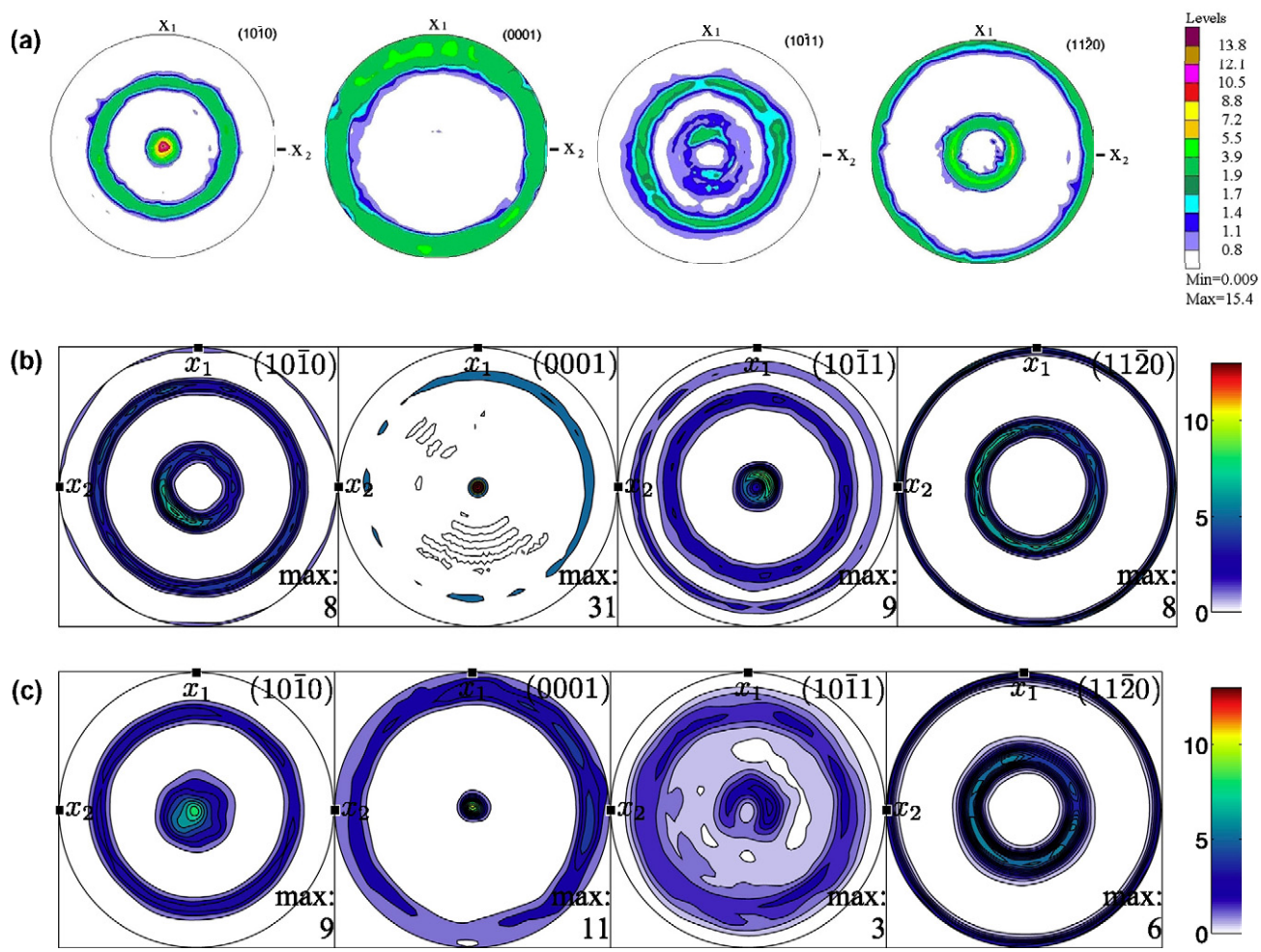

Fig. 6. (a) Experimental pole figures for nanostructured Ti after six ECAP-C passes followed by cold drawing. (b) Simulated pole figures obtained with the RVE containing 1000 crystals, each one represented by one cubic finite element. (b) Simulated pole figures obtained with the RVE containing 100 crystals, each one represented with 640 cubic finite elements.

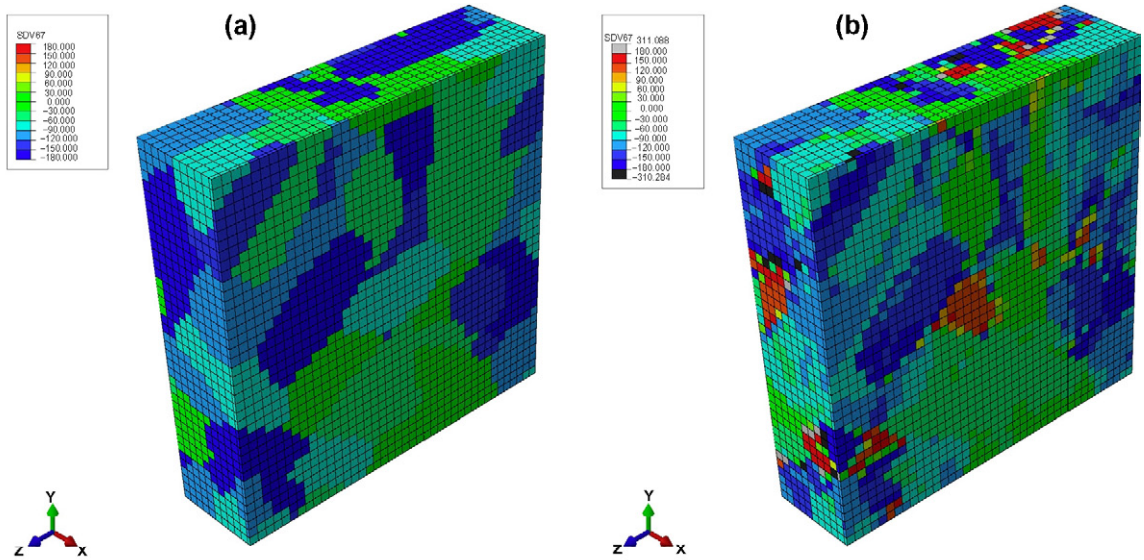

Fig. 7. Distribution of the third Euler angle in the microstructure of an RVE of polycrystalline Ti. Picture axis corresponds to $x = x_1, y = x_2$ and $z = x_3$ and contour plot is drawn on the reference configuration (a) Initial data before deformation showing the grain structure. (b) After drawing along the $z = x_3$ axis.

is represented by many finite elements. The left figure corresponds to the initial state before drawing and shows the grain structure as so all the elements belonging to the same crystal have the same orientation. Upon deformation, the local orientation changes from the crystal boundary to its interior (Fig. 7 on the right). This variation of orientation within the grains influences the pole figures but it cannot be captured if each grain is represented by one finite element, leading to the erroneous texture predictions of the texture after drawing in these latter models.

5. Conclusions

Two different homogenization approaches were used to simulate the tensile deformation and the drawing process of nanostructured Ti polycrystals. Both strategies are based on the numerical simulation of a periodic RVE of polycrystal microstructure by means of the finite element method. A single crystal plasticity model was developed to simulate the plastic deformation of nanostructured Ti by slip along the basal, prismatic and pyramidal systems. Two polycrystal representations were used for the cubic RVE. In the first one, each crystal was modeled with a single cubic finite element while many finite elements were used to model each crystal in the second one. Thus, this second approach accounted for the grain shape and size although the number of crystals within the RVE was much smaller.

The models were used to simulate a the tensile deformation of nanostructured Ti billets processed by ECAP-C. The one-voxel-one-grain model led to a slightly stiffer response (about 5%) which was traced to the poor representation of the deformation gradients within the grains by one finite element with linear displacement interpolation. This limitation of the one-voxel-one-grain model was, however, more important in the simulation of the texture evolution during drawing of nanostructured Ti billets because the experimental $(10\bar{1}0)$ fibre texture was not captured. These problems were not found in the model which include many finite element to represent each grain because the deformation gradients within each grain were adequately taken into account. Thus, in agreement with previous studies in FCC metals [35], it is concluded that a detailed resolution of the deformation fields within the nano grains is necessary to achieve an accurate prediction of the macroscopic response and, particularly, of the texture evolution. In addition, this study shows that standard crystal plasticity models can be successfully extended to nanostructured materials provided that the size effect is included in mechanical properties of single crystals.

Acknowledgement

This investigation was supported by the VINAT Project within the framework of the European Community's Seventh Framework Programme under Grant Agreement 295322. In addition, the financial support from the Spanish Ministry of Economy and Competitiveness (grant PRI-PIBUS-2011-990) through the Materials World Network programme is also gratefully acknowledged.

References

[1] R. Valiev, R. Islamgaliev, I. Alexandrov, Progress in Materials Science 45 (2) (2000) 103–189.
[2] I.J. Taylor, G.I., Metals 62 (1938) 307.
[3] R. Hill, Journal of the Mechanics and Physics of Solids 14 (2) (1966) 95–102.
[4] J. Rice, Journal of the Mechanics and Physics of Solids 19 (6) (1971) 433–455.
[5] R. Hill, J. Rice, Journal of the Mechanics and Physics of Solids 20 (6) (1972) 401–413.
[6] A. Cuitino, M. Ortiz, Engineering Computations 9 (4) (1992) 437–451.
[7] C. Miehe, International Journal for Numerical Methods in Engineering 39 (19) (1996) 3367–3390.
[8] R. Asaro, A. Needleman, Acta Metallurgica 33 (6) (1985) 923–953.
[9] J. Bassani, T. Wu, Proceedings of the Royal Society of London A 435 (1991) 2141.
[10] A. Arsenlis, D. Parks, Journal of the Mechanics and Physics of Solids 50 (9) (2002) 1979–2009.
[11] K.-S. Cheong, E. Busso, Acta Materialia 52 (19) (2004) 5665–5675.
[12] A. Ma, F. Roters, D. Raabe, Acta Materialia 54 (8) (2006) 2169–2179.
[13] J. Eshelby, Proceedings of the Royal Society of London A 252 (1957) 561–569.
[14] A. Molinari, G. Canova, S. Ahzi, Acta Metallurgica 35 (12) (1987) 2983–2994.
[15] R. Lebensohn, C. Tomé, Acta Metallurgica et Materialia 41 (9) (1993) 2611–2624.
[16] J. Segurado, R. Lebensohn, J. Llorca, C. Tomé, International Journal of Plasticity 28 (1) (2012) 124–140.
[17] J. Michel, H. Moulinec, P. Suquet, Compuational Methods in Applied Mechanics and Engineering 172 (1999) 109–143.
[18] R. Lebensohn, A. Rollett, P. Suquet, JOM 63 (3) (2011) 13–18.
[19] C. Miehe, J. Schroeder, J. Schotte, Computer Methods in Applied Mechanics and Engineering 171 (3-4) (1999) 387–418.
[20] C. Miehe, J. Schotte, M. Lambrecht, Journal of the Mechanics and Physics of Solids 50 (10) (2002) 2123–2167.
[21] Hibbit and Karlsson and Sorensen, Abaqus User's Manual v.6.7, 2007.
[22] E. Lee, D. Liu, Journal of Applied Physics 38 (1) (1967) 19–27.

[23] J. Hutchinson, Proceedings of the Royal Society of London A 348 (1976) 101–127.
[24] C. Tome, G. Canova, U. Kocks, N. Christodoulou, J. Jonas, Acta Metallurgica 32 (10) (1984) 1637–1653.
[25] E. de Souza Neto, D. Perić, D. Owen, Computational Methods for Plasticity: Theory and Applications, Wiley, 2008.
[26] S.R. Kalidindi, C.A. Bronkhorst, L. Anand, Journal of the Mechanics and Physics of Solids 40 (3) (1992) 537–569.
[27] G. Viswanathan, E. Lee, D.M. Maher, S. Banerjee, H.L. Fraser, Acta Materialia 53 (19) (2005) 5101–5115.
[28] H. Conrad, Progress in Materials Science 26 (2-4) (1981) 123–403.
[29] Q. Yu, Z.-W. Shan, J. Li, X. Huang, L. Xiao, J. Sun, E. Ma, Nature 463 (2010) 335–338.
[30] J. Gong, A. Wilkinson, Acta Materialia 57 (19) (2009) 5693–5705.
[31] A. King, M. Herbig, W. Ludwig, P. Reischig, E. Lauridsen, T. Marrow, J. Buffiere, Nuclear Instruments and Methods in Physics Research Section B: Beam Interactions with Materials and Atoms 268 (34) (2010) 291–296.
[32] Dream.3d, <http://www.dream3d.bluequartz.net>, 2012.
[33] J. Segurado, J. LLorca, Journal of the Mechanics and Physics of Solids 50 (2002) 2107–2121.
[34] D.V. Gunderov, A.V. Polyakov, I.P. Semenova, G.I. Raab, A.A. Churakova, E.I. Gimaltdinova, I. Sabirov, J. Segurado, V.D. Sitdikov, I.V. Alexandrov, N.A. Enikeev, R.Z. Valliev, Materials Science and Engineering A 562 (2013) 128–136.
[35] Z. Zhao, S. Kuchnicki, R. Radovitzky, A. Cuitio, Acta Materialia 55 (2007) 2361–2373.